



# Metal-nitrogen intimacy of the nitrogen-doped ruthenium oxide for facilitating electrochemical hydrogen production

Yeongdae Lee<sup>a,1</sup>, Jang Hyuk Ahn<sup>a,1</sup>, Seokmin Shin<sup>a</sup>, Seo-Hyun Jung<sup>b</sup>, Han-Saem Park<sup>a,2</sup>, Yoon-Gyo Cho<sup>a</sup>, Dong-Gyu Lee<sup>a</sup>, Hoyoul Kong<sup>b</sup>, Jun Hee Lee<sup>a,\*</sup>, Hyun-Kon Song<sup>a,\*</sup>

<sup>a</sup> School of Energy and Chemical Engineering, UNIST, Ulsan 44919, Republic of Korea

<sup>b</sup> Center for Advanced Specialty Chemicals, Korea Research Institute of Chemical Technology, Ulsan 44412, Republic of Korea

## ARTICLE INFO

### Keywords:

Water electrolysis  
Hydrogen evolution reaction  
Nitrogen-doped ruthenium oxides  
Mechanism  
Active sites

## ABSTRACT

In order to realize electrochemically efficient hydrogen production, various endeavors have been devoted to developing hydrogen evolution reaction (HER) electrocatalysts having zero hydrogen binding energy ( $\Delta G_{H^*} = 0$ ) for balancing between adsorption and desorption. This work demonstrated that *nitrogen* doping improved the HER activity of ruthenium oxide by letting its  $\Delta G_{H^*}$  approach zero or facilitating hydrogen desorption process. A highly nitrogen-doped ruthenium oxide catalyst guaranteeing the ruthenium-nitrogen intimacy was prepared by employing a polymer whose nitrogen-containing moiety (pyrrolidone) was *strongly* coordinated to ruthenium ion in the precursor solution prior to calcination. The less electronegative nature of nitrogen (when compared with oxygen) decreased the free energy uphill required for desorption of hydrogen intermediate species sitting on the nitrogen ( $H^*-N$  to  $1/2 H_2 + ^*N$ ) to make the desorption process more favored. Also, the nitrogen dopant facilitated  $OH^-$  desorption from its neighboring ruthenium site ( $HO^*-Ru + e^-$  to  $HO^- + ^*Ru$ ) since the less electronegative nitrogen withdrew less electrons from the ruthenium site. The ruthenium-nitrogen intimacy of the catalyst more than doubled the electrocatalytic HER current from  $33 \text{ mA cm}^{-2}$  for an undoped  $RuO_2$  to  $79 \text{ mA cm}^{-2}$  for the nitrogen-doped  $RuO_2$  at  $-50 \text{ mV}_{RHE}$ .

## 1. Introduction

Hydrogen economy has been considered to be alternative to the present carbon economy based on fossil fuels due to the environmental issues [1–4]. Hydrogen fuel benefits from its pollutant-free nature and high gravimetric energy density [5]. It sounds ridiculous that a dominant amount of hydrogen has been produced by reforming fossil fuels and therefore carbon dioxide is emitted from the hydrogen production. For holding the environmentally benign nature of hydrogen economy, it is desired to produce hydrogen from non-carbon resources [6]. Electrochemical water-splitting has been considered as a representative carbon-free hydrogen production process [7]. Efficient, stable and cost-effective electrocatalysts for both hydrogen evolution reaction (HER) and oxygen evolution reaction (OER) have been developed for improving water electrolyzers [3,8].

The electrocatalytic HER activities of catalysts have been estimated by the Gibbs free energy of the adsorption of hydrogen atom on their

active sites of the catalysts ( $\Delta G_{H^*}$ ) [9–13]. The HER exchange current density ( $j_0$ ) as a measure of the HER activity was maximized when the hydrogen adsorption and desorption were energetically and therefore kinetically balanced (i.e.,  $\Delta G_{H^*} = 0 \text{ eV}$ ). Platinum was a representative example of the nearly-zero- $\Delta G_{H^*}$  catalysts, showing high HER activity. The value of  $\Delta G_{H^*}$  of Pt(111) was estimated to be about  $-0.29 \text{ eV}$  [14]. The negative value of  $\Delta G_{H^*}$  of Pt indicated that hydrogen adsorption was more favored than hydrogen desorption. To improve the HER catalytic activity of Pt, therefore, we should let the hydrogen surface species desorbed from its active site more easily. The  $\Delta G_{H^*}$  moved in a positive direction closer to zero by employing ruthenium and its oxide favoring the desorption of the hydrogen surface species:  $\Delta G_{H^*}$  (edge) =  $-0.36 \text{ eV}$  for Pt to  $-0.33 \text{ eV}$  for Ru;  $\Delta G_{H^*}$  (terrace) =  $-0.29 \text{ eV}$  for Pt (111) to  $-0.20 \text{ eV}$  for Pt(111)Ru\* [14]. They were the easier-desorption catalysts, showing more excellent HER activities than Pt/C [15–18]. The NiTe nanorods as a support material even more improved the HER activity of  $RuO_2$  by increasing the  $\Delta G_{H^*}$  of  $RuO_2$  from  $-0.31 \text{ eV}$  to  $+0.09$

\* Corresponding authors.

E-mail addresses: [junhee@unist.ac.kr](mailto:junhee@unist.ac.kr) (J.H. Lee), [philiphobi@hotmail.com](mailto:philiphobi@hotmail.com) (H.-K. Song).

<sup>1</sup> Y.L. and J.H.A. contributed equally to this work.

<sup>2</sup> Present address: Mobility & IT Battery Division, LG Energy Solution, Daejeon 34112, Republic of Korea.

eV and therefore facilitating  $H_2$  desorption [18]. However, there is still room for improving  $\Delta G_H^*$  toward zero.

Nitrogen-containing active sites have been presented since Jasinski used cobalt phthalocyanine (Co-N<sub>4</sub>) as the molecular catalyst for oxygen reduction reaction (ORR) in 1964 [19]. Following the study on the metal-N<sub>4</sub> macrocycles, the metal-N-C catalysts for ORR were proposed [20]. They were prepared by pyrolyzing (1) the metal-N<sub>4</sub> macrocycles adsorbed on carbon supports or (2) the mixtures of metal, nitrogen and carbon precursors. Even without the metal component, the nitrogen-doped carbon nanotube arrays [21] and graphene [22] showed high electrocatalytic activity of ORR. Also, the catalysts with nitrogen-containing active sites worked successfully for HER: metal-N<sub>4</sub> [23], metal-N-C [24,25] and nitrogen doped carbon [26].

In this work, we doped ruthenium oxide as the HER catalyst with nitrogen to make  $\Delta G_H^*$  of RuO<sub>2</sub> approach zero for improving its HER activity. The nitrogen-doped RuO<sub>2</sub> (N-RuO<sub>2</sub>) guaranteeing the Ru-N intimacy was obtained by pyrolyzing the polymer with the nitrogen-containing group chelating ruthenium ion. The superiority of the nitrogen-doped RuO<sub>2</sub> over bare RuO<sub>2</sub> and Pt was clearly and experimentally demonstrated. The density functional theory (DFT) calculation proposed a dual active center mechanism for HER by the N-RuO<sub>2</sub>. A water molecule was split in alkaline media after it was bound on two active centers of \*Ru and \*N to form HO-\*Ru and H-\*N. Hydrogen was produced from H-\*N while OH<sup>-</sup> was generated from HO-\*Ru. The surface nitrogen (\*N) of N-RuO<sub>2</sub>, electron-poorer than the \*O of RuO<sub>2</sub>, bound proton weaker so that  $\Delta G_H^*$  went to a more positive value closer to the energy of the desorbed state for hydrogen evolution from -0.56 eV for \*O to -0.25 eV for \*N. Moreover, the \*Ru of N-RuO<sub>2</sub>, electron-richer than that of undoped RuO<sub>2</sub>, released OH<sup>-</sup> in an easier way because the nitrogen dopant withdrew less electrons of the surface ruthenium than the surface oxygen did.

## 2. Experimental section

### 2.1. Pyrd-PVA-CN

PVA-CN (cyanoethyl polyvinyl alcohol; Shin-Etsu Chemical, CRV) was functionalized by a pyrrolidone-containing moiety [27]. The PVA-CN polymer consisted of 24 mol. % alcoholic units and 76 mol. % cyanoethyl units. The alcoholic groups were replaced by the pyrrolidone-containing moiety. PVA-CN (7 g or 0.039 mol), dicyclohexylcarbodiimide (DCC, 11.7 g or 0.057 mol) and 2-pyrrolidone-5-carboxylic acid (7.4 g or 0.057 mol) were added sequentially into a 250-mL round-bottomed flask with 65 mL dimethylformamide (DMF). 4-dimethylaminopyridine (DMAP; 0.29 g or 2.4 mmol) in 25 mL of DMF was slowly introduced dropwise into the reactant-containing flask immersed in an ice-water bath. The reaction mixture was stirred at 30 °C for 8 h. Insoluble DCC urea precipitated during the reaction was removed by filtration. The polymer product in the filtrate solution was precipitated by introducing ethanol into the filtrate solution. The excess 2-pyrrolidone-5-carboxylic acid was removed from the solid product. The polymer product was purified twice more via dissolving it in acetone, precipitating it in ethanol and drying it under vacuum at 100 °C for 24 h.  $M_n = 135,000$ ;  $M_w/M_n = 4.14$ . <sup>1</sup>H NMR (300 MHz, DMSO-d<sub>6</sub>,  $\delta$  in ppm): 7.8 (1H, s, CH-NH-C=O), 5.03 (1H, s, CH<sub>2</sub>-CH-O-(C=O)), 4.71 (1H, s, -O-(C=O)-CH), 4.38 (1H, s, CH<sub>2</sub>-CH-OH), 3.63 (3H, s, O-CH<sub>2</sub>-CH<sub>2</sub>, CH<sub>2</sub>-CH-OH), 2.71 (2H, s, CH<sub>2</sub>-CH<sub>2</sub>-CN), 2.25–1.2 (CH<sub>2</sub>-CH-O-CH<sub>2</sub>, -CH<sub>2</sub>-CH-O-(C=O)-, CH<sub>2</sub>-CH-OH).

### 2.2. Catalysts

Pyrd-PVA-CN, PVA-CN and PVA were used as the polymer precursor for synthesizing N<sub>0.9</sub>-RuO<sub>2</sub>@NC, N<sub>0.5</sub>-RuO<sub>2</sub>@NC and RuO<sub>2</sub>@C, respectively. 100 mg polymer was dispersed in 10 mL dimethyl sulfoxide at 80 °C for 3 h. 50 mg RuCl<sub>3</sub> was dissolved in the polymer dispersion at room temperature for 24 h. The metal/polymer precursor mixture was freeze-

dried for 1 day (FDCF-12012, Operon). The dried mixture was calcined in air at 300 °C for 3 h with 5 °C per minute ramping. The calcined product was purified by dispersing in excess water followed by centrifuging at 10,000 rpm for 3 min 3 times and filtrating. The purified product was freeze-dried for 1 day.

### 2.3. Characterization

<sup>1</sup>H nuclear magnetic resonance (NMR) spectra of polymers in DMSO-d<sub>6</sub> were collected by a nuclear magnetic resonance (NMR) spectrometer (Bruker Avance 300 MHz). The apparent molecular weights ( $M_n$ ) and molecular weight distributions ( $M_w/M_n$ ) were measured at 1 mL min<sup>-1</sup> dimethylformamide (DMF) eluent at 30 °C with a polymethylmethacrylate (PMMA) standard by gel permeation chromatography (GPC; Agilent Technologies 1200 series). Images, electron diffraction patterns, and energy-dispersive X-ray spectra (EDS spectra) were obtained by a transmission electron microscope (TEM; JEOL JEM-2100F). X-ray diffraction (XRD) patterns were acquired using an XRD diffractometer (Rigaku D/MAX2500V/PC) with a copper rotating-anode X-ray operating at 40 kV and 200 mA. Ru 3p and N 1s X-ray photoelectron spectra (XPS; Thermo Fisher K-alpha) were fitted with a mixed function of 80% Gaussian and 20% Lorentzian after subtracting the Shirley background from the spectra. The beam line 6D of the Pohang Accelerator Laboratory (PAL) was used for X-ray absorption spectroscopy (XAS). The operating voltage of the accelerator was 3.5 GeV while the current was 400 mA. The samples were prepared by pelletizing catalyst powder to 240  $\mu$ m-thick pellets on a 3 M tape. The signals were detected in the transmission and fluorescence modes.

### 2.4. Electrochemical characterization

A mixture of 10 mg ruthenium oxide catalyst and 2.5 mg Ketjen black or 10 mg Pt/C (ETEK, 20 wt%) was dispersed in a mixture of 1 mL ethanol and 50  $\mu$ L 5 wt% Nafion in an ethanol/water mixture (45 wt% water). The suspension was sonicated for 30 min 5  $\mu$ L of the suspension was cast on the 0.1256 cm<sup>2</sup> disk of a rotating ring-disk electrode (RRDE). The catalyst-loading RRDE was used as the working electrode while a graphite rod (diameter = 6.15 mm, Alfa Aesar) and a Hg/HgO were used as the counter and reference electrodes, respectively. A 1 M KOH solution was used as the alkaline medium. The RRDE was rotated at 1600 rpm in a three-electrode configuration. HER polarization curves were obtained in the argon-purged electrolyte by scanning the potential at 5 mV s<sup>-1</sup> from 0.1 V<sub>RHE</sub> to -0.2 V<sub>RHE</sub>. The potential was swept 10,000 times at 50 mV s<sup>-1</sup> between -0.1 V<sub>RHE</sub> and 0.1 V<sub>RHE</sub> in the argon-purged electrolyte for estimating the durability of the HER activity. All HER polarization curves were ir-compensated at 85%.

## 3. Results and discussion

### 3.1. Nitrogen-doped ruthenium oxide (N<sub>x</sub>-RuO<sub>2</sub>)

The metal-N<sub>4</sub> macrocycles have been often used as the co-precursors of metal and nitrogen to prepare metal-N-C catalysts [28–31]. There is every possibility that the metal-nitrogen complex co-precursors guarantee the metal-nitrogen intimacy in the metal-N-C catalysts even if individual precursors of metal and nitrogen have been popularly used for saving the cost of the expensive macrocycle compounds. As another example of the use of metal-nitrogen complex for nitrogen doping, titanium oxide (equivalent to ruthenium oxide in terms of its rutile structure [32]) was successfully nitrogen-doped by calcining polyvinylpyrrolidone-titanium ion complex [33]. Inspired by the uses of the metal-nitrogen complexes for making the metal-nitrogen intimacy, we designed the synthesis process to have the strong interaction between metal and nitrogen precursors in the precursor solution for making the nitrogen-doped ruthenium oxide.

Pyrrolidone-functionalized cyanoethyl polyvinyl alcohol (Pyrd-PVA-

CN in Fig. 1a;  $^1\text{H}$  NMR fingerprint in Fig. S1 [27,34,35] was used as the nitrogen precursor polymer. The nitrogen of pyrrolidone (Pyrd) unit was expected to be strongly coordinated to ruthenium ion for guaranteeing the ruthenium/nitrogen intimacy [36]. Density function theory (DFT) calculation suggested that a divalent transition metal ion triply coordinated to (1) the nitrogen of pyrrolidone hetero ring, (2) the oxygen of carbonyl group of pyrrolidone and (3) the oxygen of ester groups in the bridge between pyrrolidone and vinyl backbone of PVA-CN [27]. Cyanoethyl polyvinyl alcohol (PVA-CN) was used as the nitrogen-containing weak-coordination precursor for comparison [37]. Polyvinyl alcohol (PVA) was used as the no-coordination precursors without nitrogen contents.

The nitrogen-doped ruthenium oxide catalyst embedded in nitrogen-doped carbon matrix ( $\text{N}_{0.9}\text{-RuO}_2\text{@NC}$ ) was prepared by calcining the mixture of a ruthenium precursor and the strong-coordination Pyrd-PVA-CN at  $300^\circ\text{C}$  for 3 h (Fig. 1a). The subscript number of N for nitrogen,  $x$ , indicated the number of nitrogen atoms coordinated to a single ruthenium atom. The coordination number  $x$  was used as a measure of the ruthenium-nitrogen intimacy in this work. We discussed how to estimate the number below. The Ru-N intimate pair in the precursor mixture was thought to be converted to the nitrogen-doped ruthenium oxide ( $\text{N}_x\text{-RuO}_2$ ). That is to say, the nitrogen dopant was thought to come dominantly from Pyrd moiety. The PVA backbone containing cyanoethyl functionality was thought to be converted to the nitrogen-doped carbon (NC). In the same way, the less-nitrogen-doped counterpart ( $\text{N}_{0.5}\text{-RuO}_2\text{@NC}$ ) was prepared from the weak-coordination PVA-CN while the nitrogen-free control ( $\text{RuO}_2\text{@C}$ ) was obtained in the presence of the no-coordination PVA.

All prepared catalyst/matrix hybrids had the 1-to-3-nm  $\text{RuO}_2$  nano-islands loaded on carbon matrix (transmission electron microscope (TEM) images in Figs. 1b and S2). The material identity of the  $\text{RuO}_2$

nano-islands was clearly identified by the lattice periodicity shown in the crystallographic fringes, its Fourier-transformed diffraction patterns (Figs. 1c and S3) and X-ray diffraction patterns (Fig. S4). Tetravalency of ruthenium ( $\text{Ru}^{4+}$ ) was dominant for all samples, which was indicated by the peaks of  $3p_{3/2}$  and  $3p_{1/2}$  in Ru3p spectra of X-ray photoelectron spectroscopy (XPS in Fig. S5) [38]. Nitrogen element was found on the  $\text{RuO}_2$  nano-islands as well as the carbon matrix of  $\text{N}_x\text{-RuO}_2\text{@NC}$  and  $\text{RuO}_2\text{@C}$  as indicated in the energy-dispersive spectroscopy (EDS) 2D images (Figs. 1d, S6 and S7).

### 3.2. Ruthenium-nitrogen intimacy

The Ru-N intimacy in  $\text{N}_{0.9}\text{-RuO}_2$  originated from the strong coordination of ruthenium ion to the pyrrolidonic nitrogen in the precursor solution before calcination. The quartz crystal microbalance (QCM) confirmed the adsorption of ruthenium ion on Pyrd moiety of Pyrd-PVA-CN (Fig. 2a). The Pyrd-PVA-CN showed the most significant frequency decrease (indicating the most significant mass increase) among the tested polymers. However, no evident changes in frequency were observed with PVA and PVA-CN. The comparison between the polymers supported that  $\text{Ru}^{3+}$  was adsorbed not on alcoholic and cyanoethyl groups but on Pyrd moiety.

The amount of the N coordinated to Ru (Ru-N) was calculated from the N1s X-ray photoelectron spectra (XPS spectra in Fig. 2b and c; and Fig. S8). The spectra were deconvoluted by the elementary spectra of four possible nitrogen species including the Ru-N as well as pyrrolic, pyridinic and quaternary N. 9 at% (atomic percentage) of the total amount of nitrogen was bound to Ru in the N-doped  $\text{RuO}_2$  rooting from the strong-coordination Pyrd-PVA-CN ( $\text{N}_{0.9}\text{-RuO}_2\text{@NC}$  in Fig. 2b). The 91 at% N was thought to be placed on the carbon matrix (NC) as a form of pyrrolic, pyridinic and quaternary N. The nitrogen in the carbon

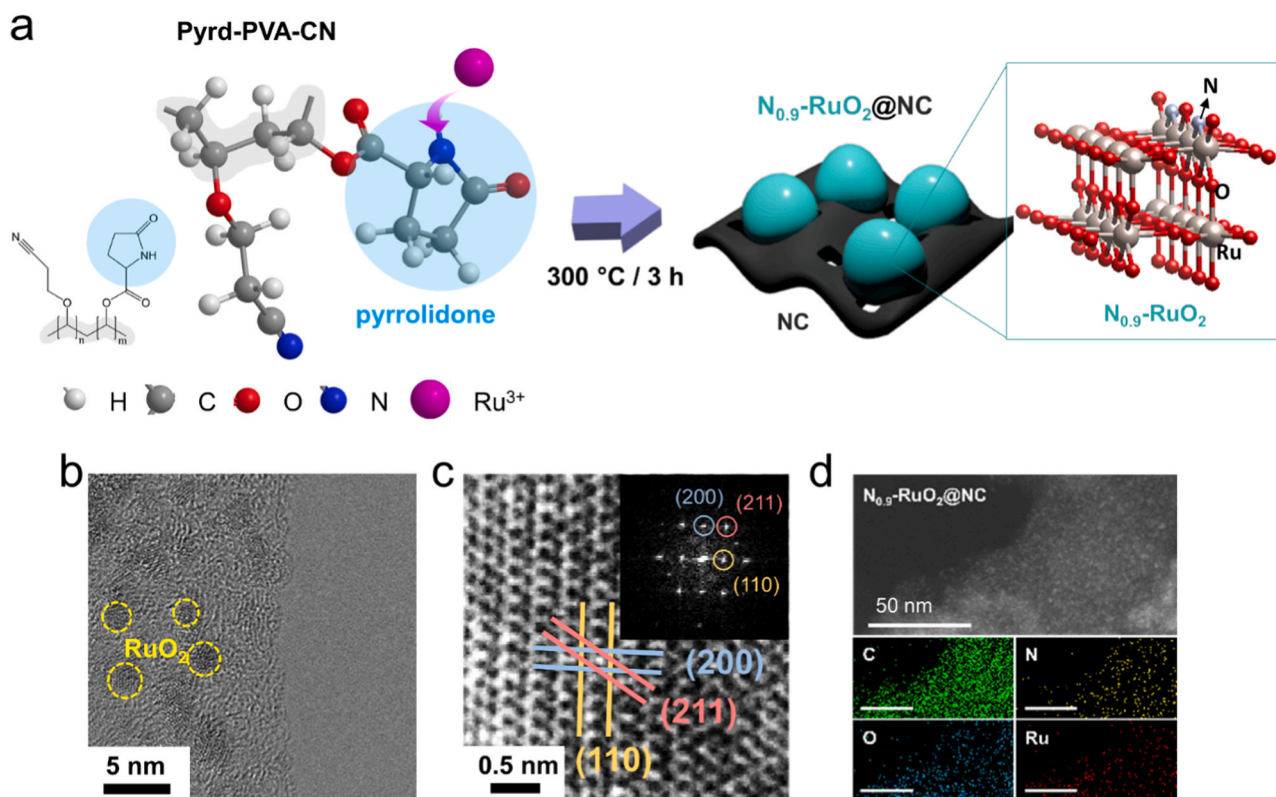


**Fig. 1.** Highly nitrogen-doped ruthenium oxide catalyst,  $\text{N}_{0.9}\text{-RuO}_2\text{@NC}$ . (a) Preparation of  $\text{N}_{0.9}\text{-RuO}_2\text{@NC}$  from pyrrolidone-functionalized cyanoethyl polyvinyl alcohol (Pyrd-PVA-CN) strongly coordinated ruthenium ion. (b and c) High-resolution transmission electron microscope (HR-TEM) images of  $\text{N}_{0.9}\text{-RuO}_2\text{@NC}$  and  $\text{N}_{0.9}\text{-RuO}_2$  nano-islands. Inset in c: A fast Fourier transform (FFT) pattern of c. (d) Two-dimensional element maps by energy dispersive spectroscopy with scanning transmission electron microscopy (STEM-EDS). Scale bar = 50 nm.

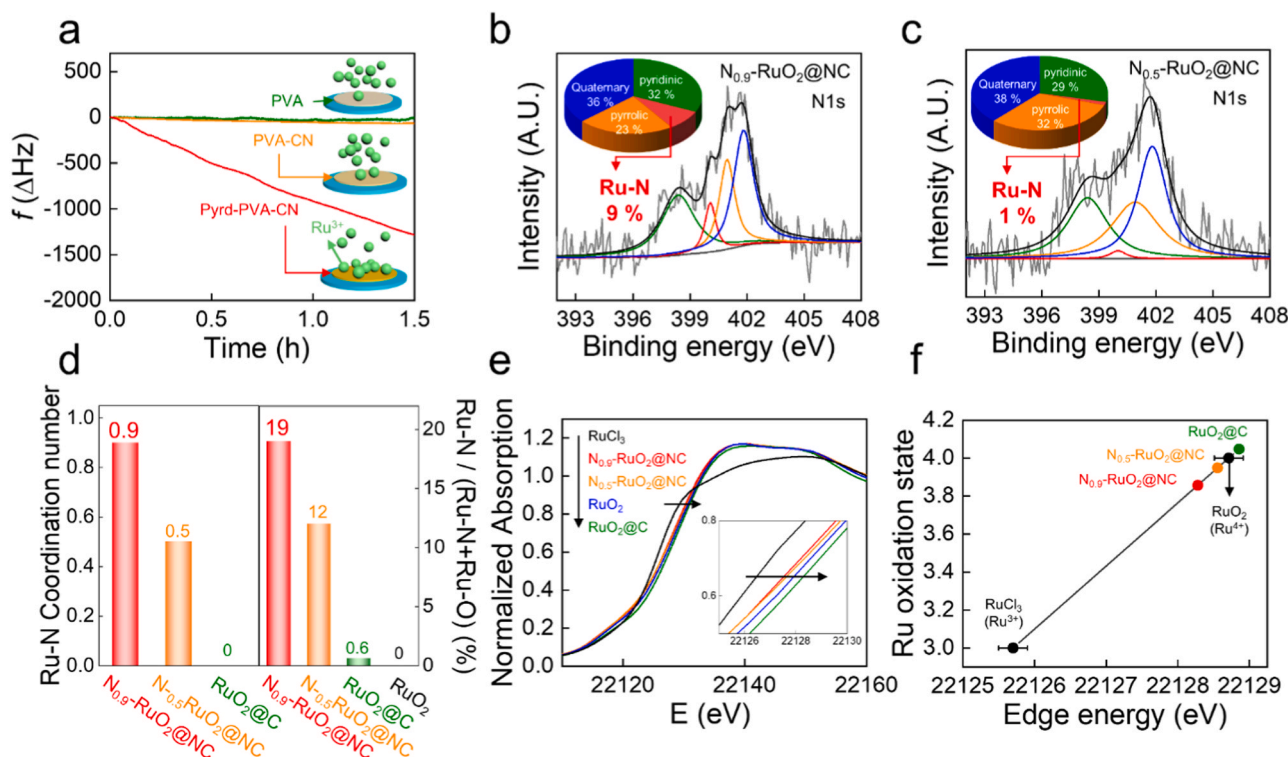


**Fig. 2.** Nitrogen doping of ruthenium oxide. (a) Temporal frequency ( $f$ ) change of polymers loaded on the gold-coated quartz crystal resonators of quartz crystal microbalance (QCM) in 2000 ppm  $\text{Ru}^{3+}$  aqueous solution. Polymers loaded on the resonators were dried at 80 °C for 1 h before the measurement. (b and c) N 1s X-ray photoelectron spectra (XPS). The spectra were deconvoluted by the elemental spectra of pyridinic N (green), pyrrolic N (orange), quaternary N (blue) and Ru-N (red). The portion of each elemental spectra over the full spectra was indicated in the pie chart. (d) Ru-N coordination numbers calculated by fitting extended X-ray absorption fine structure (EXAFS) (left); the ratio of the mass of Ru-N to (Ru-N + Ru-O) induced by the matrix-assisted laser desorption/ionization/time-of-flight/mass spectrometer (MALDI/TOF/MS) (right). (e) X-ray absorption near edge structure (XANES) spectra. Inset: Magnified spectra between 22,125 eV and 22,130 eV. (f) Linear correlation between the oxidation states of Ru and the edge energy of d.

matrix was expected to originate from the non-coordinating Pyrd and the cyanoethyl functionality of the Pyrd-PVA-CN. On the other hand, only 1 at% of the total amount of nitrogen was the ruthenium-coordinating nitrogen in the N-doped  $\text{RuO}_2$  prepared from PVA-CN without the metal-chelating Pyrd moiety ( $\text{N}_{0.5}\text{-RuO}_2\text{@NC}$  in Fig. 2c). The Ru-N pairing was not very expected due to the absence of Pyrd so that the amount of nitrogen coordinated to ruthenium decreased significantly. As expected, the nitrogen was not detected in  $\text{RuO}_2\text{@C}$  prepared from the nitrogen-absent polymer (Fig. S8). Simultaneously, the oxygen content bound to ruthenium (O of Ru-O) decreased as the Ru-N pairing increased (O 1s XPS spectra in Fig. S9). Only 2.3 at% of the amount of total elements was dedicated to Ru-O in the highest-nitrogen-content  $\text{RuO}_2$  ( $\text{N}_{0.9}\text{-RuO}_2\text{@NC}$ ) while 3.6 at% for  $\text{N}_{0.5}\text{-RuO}_2\text{@C}$  and 4.1 at% for  $\text{RuO}_2\text{@C}$  [39]. The tradeoff between N and O indicates that a portion of the lattice oxygen of  $\text{RuO}_2$  was replaced by nitrogen when nitrogen was doped in  $\text{RuO}_2$ . When the 4.1 at% of the undoped  $\text{RuO}_2\text{@C}$  was equivalent to the stoichiometry of Ru to O in  $\text{RuO}_2$ , the nitrogen coordination number of  $\text{N}_{0.9}\text{-RuO}_2\text{@NC}$  was calculated to be 0.9, identical to the subscript value of N estimated by X-ray absorption spectra below.

The fine structures of the synthesized ruthenium oxide catalysts were investigated by X-ray. Radial distribution functions (RDFs) were obtained by Fourier-transforming the  $k^3$ -weighted extended X-ray absorption fine structure (EXAFS) spectra (Fig. S10). Coordination numbers and radial distances of Ru-O and Ru-N were calculated by fitting the RDFs in the R-space (Fig. 2d, Fig. S11, and Table S1). The coordination number (CN) of Ru-N (Ru-N CN;  $x$  in  $\text{N}_x\text{-RuO}_2$ ) was the average number of N coordinated to a single Ru. As expected, the N-doped  $\text{RuO}_2$  rooting from the strong-coordination Pyrd-PVA-CN showed the highest value of the Ru-N CN ( $x = 0.9$ ;  $\text{N}_{0.9}\text{-RuO}_2\text{@NC}$ ). Almost

every lattice Ru was coordinated to a single nitrogen dopant in the  $\text{N}_{0.9}\text{-RuO}_2\text{@NC}$ . Therefore, we confirmed that our strategy based on the strong coordination of the N of Pyrd to Ru worked successfully. Without the metal-chelating Pyrd moiety, the CN value fell down to 0.5 for the N-doped  $\text{RuO}_2$  prepared from PVA-CN ( $\text{N}_{0.5}\text{-RuO}_2\text{@NC}$ ). One of two Ru atoms was coordinated to a nitrogen dopant in the  $\text{N}_{0.5}\text{-RuO}_2\text{@NC}$ .

Total CN including Ru-N as well as Ru-O was estimated to be around 4 for all samples including undoped and nitrogen-doped ruthenium oxides (Table S1). Even if the tetra-coordination did not meet the octahedral structure of rutile  $\text{RuO}_2$  bulk, the less coordination resulted from its nano-dimensional nature (1–2 nm in Figs. 1b and S1) of having a significant portion of surface with non-stoichiometric bonds. The similar case was found in the case of  $\text{TiO}_2$  nanoparticles in rutile phase: the Ti-O CN decreased from 6 for 20 nm particle to 5 for 5 nm to 4 for 3 nm [40]. The Ru-N CN and the Ru-O CN were traded off (Table S1): higher Ru-N CN brought lower Ru-O CN. It suggested that the nitrogen was doped into the place of the lattice O. The nitrogen doping increased the radial distance between Ru and its neighboring atom (O before the N doping) due to the atomic radius of N larger than O (the right shift of the peak at  $\sim 0.15$  nm in RDFs of Fig. S10). In the same reason, the d-spacing of  $\text{RuO}_2$  (211) also increased as more nitrogen atoms were doped (XRD in Fig. S4):  $\text{RuO}_2$  (1.690 Å)  $\approx$   $\text{RuO}_2\text{@C}$  (1.690 Å)  $<$   $\text{N}_{0.5}\text{-RuO}_2\text{@NC}$  (1.693 Å)  $<$   $\text{N}_{0.9}\text{-RuO}_2\text{@NC}$  (1.697 Å).

The Ru-N fragments of  $\text{N}_x\text{-RuO}_2\text{@NC}$  were detected by the matrix-assisted laser desorption/ionization / time-of-flight / mass spectrometer (MALDI/TOF/MS in Fig. S12). Therefore, the existence of the Ru-N coordination indicating the Ru-N intimacy was confirmed. Seven different Ru isotopes available in nature were identified for all samples, showing an identical composition of  $^{96}\text{Ru}$  (5.4%),  $^{98}\text{Ru}$  (1.9%),  $^{99}\text{Ru}$  (12.8%),  $^{100}\text{Ru}$  (12.6%),  $^{101}\text{Ru}$  (17.1%),  $^{102}\text{Ru}$  (31.6%) and  $^{104}\text{Ru}$

(18.6%) (Fig. S12a; Supporting information for calculation). The combinations of the Ru isotopes with  $^{14}\text{N}$  or  $^{16}\text{O}$  were found in the range between 110 ( $^{96}\text{Ru} + ^{14}\text{N}$ ) and 120  $m/z$  ( $^{104}\text{Ru} + ^{16}\text{N}$ ) (Fig. S12b). The isotopes of N and O were ignored due to its rare population in nature. In the absence of nitrogen dopant, the peak intensity of  $\text{RuO}_2$  decreased along  $^{102}\text{Ru} + ^{16}\text{O}$  at 118 to  $^{101}\text{Ru} + ^{16}\text{O}$  at 117 to  $^{100}\text{Ru} + ^{16}\text{O}$  at 116 ( $\text{RuO}_2$  and  $\text{RuO}_2@\text{C}$  in Fig. S12b), following the abundance order of Ru in the  $m/z$  range of 100–102 (Fig. S12a). For the nitrogen-doped ruthenium oxides, however, the monotonically decreasing peak intensity order along 118–116 was broken: the peaks at 116 were more intensified than those at 117. It allowed us to guess that the nitride ( $^{14}\text{N}$ ) of the most abundant  $^{102}\text{Ru}$  was responsible for the intensity increase at 116. Therefore, we calculated the number ratio of Ru-N to (Ru-N + Ru-O) by using the peak intensities at 116 and 117: Ru-O from 117 and (Ru-N + Ru-O) from 116 (Supporting information for calculation). The N was involved in 12% and 19% of the total number of bonds of Ru in  $\text{N}_{0.5}\text{-RuO}_2@\text{NC}$  and  $\text{N}_{0.9}\text{-RuO}_2@\text{NC}$ , respectively (Figs. 2d and S12c). The values coincided with the ratio of the coordination number calculated by EXAFS, (Ru-N CN)/(Ru-N CN + Ru-O CN): 13% for  $\text{N}_{0.5}\text{-RuO}_2@\text{C}$  and 22% for  $\text{N}_{0.9}\text{-RuO}_2@\text{C}$  (Table S1).

The oxidation state of ruthenium changed with the amount of nitrogen dopant (X-ray absorption near edge structure or XANES in Fig. 2e) [41]. The first inflection point on the K edge of the XANES spectra of ruthenium oxide determined the oxidation state of ruthenium [42]. The edge energies of the nitrogen-doped ruthenium oxides were found between  $\text{RuCl}_3$  ( $\text{Ru}^{3+}$ ) and  $\text{RuO}_2$  ( $\text{Ru}^{4+}$ ), indicating their oxidation states between 3 and 4. The nitrogen dopant decreased the oxidation state of Ru from +4.05 for  $\text{RuO}_2@\text{C}$  to +3.95 for  $\text{N}_{0.5}\text{-RuO}_2@\text{NC}$  to +3.86 for  $\text{N}_{0.9}\text{-RuO}_2@\text{NC}$  (Fig. 2f). The less electronegative N (electronegativity = 3.04) withdrew less electrons from Ru (2.2) than O (3.44) did.

### 3.3. Hydrogen evolution reaction (HER)

The HER activities were measured by the linear sweep voltammetry using the rotating ring-disk electrode in 1 M KOH (aq). The calcination

temperature for the nitrogen-doped ruthenium oxide catalysts was optimized between 200 °C and 450 °C to maximize the HER activities. The catalysts calcined at 300 °C showed the highest HER activities for both Pyrd-PVA-CN and PVA-CN (Figs. S13 and S14). The XANES data supported that the ruthenium precursor ( $\text{Ru}^{3+}$ ) was not sufficiently oxidized at the temperatures lower than 300 °C: the trivalent ruthenium was dominantly left after the calcination (Fig. S15). On the other hand, the calcination above 300 °C fully oxidized the ruthenium precursor and increased the oxidation state of Ru to the values higher than +3.86 (the oxidation state at 300 °C). However, the over-oxidation decreased the amount of nitrogen dopant and resultantly the HER activity (Fig. S13, S14 and S16). Therefore, the calcination temperature was fixed at 300 °C for all samples.

The HER activities of the nitrogen-doped  $\text{RuO}_2$  with nitrogen-doped carbon matrix ( $\text{N}_x\text{-RuO}_2@\text{NC}$ ) prepared at the optimized condition were compared with the controls including the bare  $\text{RuO}_2$ , Pt/C and  $\text{RuO}_2@\text{C}$  prepared from PVA (Fig. 3a). The bare  $\text{RuO}_2$  was inferior to Pt/C in terms of the HER activity. When the carbon matrix was introduced to  $\text{RuO}_2$  by calcination in the presence of PVA, the HER activity of  $\text{RuO}_2@\text{C}$  was improved to be higher than that of Pt/C. More importantly, the nitrogen doping improved the HER activity of  $\text{RuO}_2$  significantly. As the Ru-N intimacy increased, the HER activity was more improved. The HER activity of the series of  $\text{RuO}_2$  catalysts was strongly dependent on the Ru-N intimacy. The Ru-N intimacy dependency was clearly visualized by plotting the HER activity against the Ru-N CN (Fig. 3b and c; Fig. S17). The Ru-N CN was considered as not only a measure of the Ru-N intimacy but also the catalyst descriptor. The HER activity was represented by (1) the current density at  $-50$  mV versus reversible hydrogen electrode (RHE), (2) the overpotential ( $\eta$ ) at  $-10$  mA  $\text{cm}^{-2}$ , (3) the Tafel slope ( $b$ ) and (4) the exchange current ( $i_0$ ). As the Ru-N CN increased, all measures of the HER activity were improved: the currents increased while the overpotential and the Tafel slope decreased. As a summary, the HER activity followed the descending order of  $\text{N}_{0.9}\text{-RuO}_2@\text{NC} > \text{N}_{0.5}\text{-RuO}_2@\text{NC} > \text{RuO}_2@\text{C} > \text{Pt/C} > \text{RuO}_2$ . Our best  $\text{N}_{0.9}\text{-RuO}_2@\text{NC}$  was competitive at the top-tier level in terms of the HER activity among the previously reported works including precious and non-precious metals

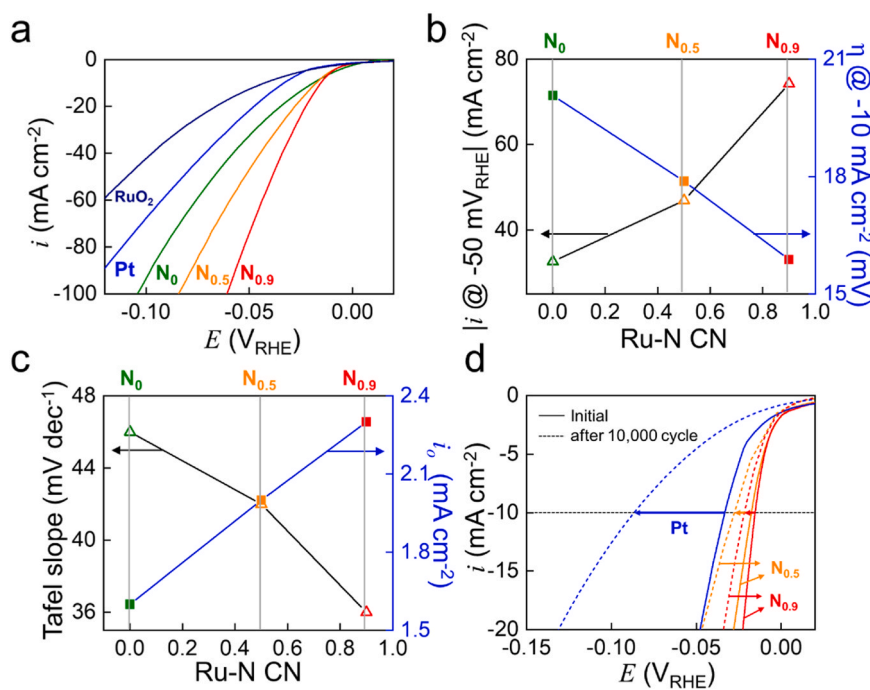


**Fig. 3.** HER activity.  $\text{N}_{0.9} = \text{N}_{0.9}\text{-RuO}_2@\text{NC}$ ;  $\text{N}_{0.5} = \text{N}_{0.5}\text{-RuO}_2@\text{NC}$ ;  $\text{N}_0 = \text{RuO}_2@\text{C}$ ; Pt = Pt/C. (a) HER polarization curves at 1600 rpm in 1 M KOH. (b) Current densities at  $-50$  mV<sub>RHE</sub> ( $|i| @ -50 \text{ mV}_{\text{RHE}}$ ) and overpotentials ( $\eta$ ) at  $-10$  mA  $\text{cm}^{-2}$  as functions of the Ru-N coordination number (Ru-N CN). (c) Tafel slopes and exchange currents ( $i_0$ ) as functions of the Ru-N. (d) Catalyst durability test. HER activities were compared between before and after 10,000 HER cycles.

and their compounds as the HER catalysts (Fig. S18; Table S2).

In addition to the HER activity, all of the RuO<sub>2</sub> catalysts were superior to Pt/C in terms of HER durability. More importantly, the HER durability was improved as the Ru-N intimacy increased. When potential was swept repeatedly, the potential required for HER at  $-10 \text{ mA cm}^{-2}$  was shifted only by 6 mV for N<sub>0.9</sub>-RuO<sub>2</sub>@NC and 12 mV for N<sub>0.5</sub>-RuO<sub>2</sub>@NC after 10,000 cycles (N<sub>0.9</sub> and N<sub>0.5</sub> in Fig. 3d, respectively). These overpotentials were considered to be insignificant given that the HER polarization curve of Pt/C was seriously shifted by 54 mV (Pt in Fig. 3d). In the potentiostatic cycles at 20 mV<sub>RHE</sub>, also, the similar durability improvement trend was observed: the higher the nitrogen doping content, the better the durability (N<sub>0.9</sub> > N<sub>0.5</sub> > N<sub>0</sub> in Fig. S19). The serious HER activity decay of Pt/C indicated by the overpotential increase (Pt in Fig. 3d) has been known to be due to serious electroactive surface area decrease of Pt caused by catalyst loss and agglomeration [43–45]. On the other hand, the particle size change of all RuO<sub>2</sub> catalysts used in this study was not serious after 10,000 cycles, confirming less serious catalyst agglomeration (Fig. S20). When the particle size change after 10,000 cycles was compared between the RuO<sub>2</sub> catalysts, more interestingly, higher Ru-N intimacy guaranteed less significant change of particle size. The difference of population of particles larger than 4 nm between before and after cycles was: 3% for N<sub>0.9</sub> < 5% for N<sub>0.5</sub> < 19% for N<sub>0</sub> (Fig. S20). Therefore, we guess that the strong Ru-NC interaction between ruthenium atom of RuO<sub>2</sub> and nitrogen atom of the nitrogen-doped carbon made the big difference of the size change between N-doped (N<sub>0.9</sub> and N<sub>0.5</sub>) and N-undoped RuO<sub>2</sub> (N<sub>0</sub>). The strong catalyst/support interaction cases resulting in improved catalyst durability were found in our previous works [46–48]. The Ru-N bond in nitrogen-doped ruthenium oxide, which is known to be more stable or stronger than Ru-O bond [49], could be the next factor to improve the durability. Such strong interactions of Ru-NC and Ru-N were expected to keep the integrity of catalyst particles and disallow metal atoms in RuO<sub>2</sub> to be dissolved.

### 3.4. Electron re-distribution induced by nitrogen doping

The density function theory (DFT) calculation was used to identify the active sites of the nitrogen-doped ruthenium oxide (N-RuO<sub>2</sub>) and reveal how the nitrogen dopant improved the HER activity. Three different oxygen atoms were coordinated to the surface ruthenium of RuO<sub>2</sub> rutile (Fig. S21). The lattice oxygen (O<sub>Lattice</sub>) having its coordination to three ruthenium atoms (coordination number, CN = 3) connected the surface ruthenium with the lattice ruthenium in the bulk. The surface oxygen (O<sub>Surface</sub>) in the surface plane of RuO<sub>2</sub> was coordinated to three surface ruthenium atoms (CN = 3). The bridging oxygen (O<sub>Bridge</sub>) out of the surface plane as the third type bridged two surface ruthenium atoms (CN = 2). More energy was required for replacing the O<sub>Surface</sub> by nitrogen to form N<sub>Surface</sub>-RuO<sub>2</sub> when compared with the bulk doping (N<sub>Lattice</sub>-RuO<sub>2</sub>) and the surface doping via replacing O<sub>Bridge</sub> (N<sub>Bridge</sub>-RuO<sub>2</sub>) (Fig. S22). The N<sub>Bridge</sub>-RuO<sub>2</sub> was used as the model structure for calculation because the lattice nitrogen in bulk was not able to participate in HER (Fig. 4a). The hydrogen binding energies ( $\Delta G_H$ ) were compared between the nitrogen, oxygen and ruthenium sites on the surface of N<sub>Bridge</sub>-RuO<sub>2</sub> (Fig. S23): the  $\Delta G_H$  increased along O<sub>Bridge</sub> (−0.62 eV), N<sub>Bridge</sub> (−0.25 eV) and Ru<sub>CUS</sub> (+0.51 eV; CUS = coordinatively unsaturated sites in Fig. 4a). The oxygen site was most favored for the hydrogen adsorption while the adsorption was not easily allowed on the ruthenium site. The strong hydrogen adsorption on the oxygen site was expected to make the hydrogen desorption leading to HER difficult. The  $\Delta G_H$  of the nitrogen site was estimated to be in-between and most close to the values of the free energies of the states before adsorption and after desorption. Therefore, the nitrogen site was more appropriate for HER than oxygen and ruthenium sites due to its thermodynamic balance of the binding energy between adsorption and desorption.

Considering that the hydrogen adsorption was more favorable on oxygen and nitrogen rather than ruthenium, a HER mechanism in alkaline media was constructed:

#### Adsorption.

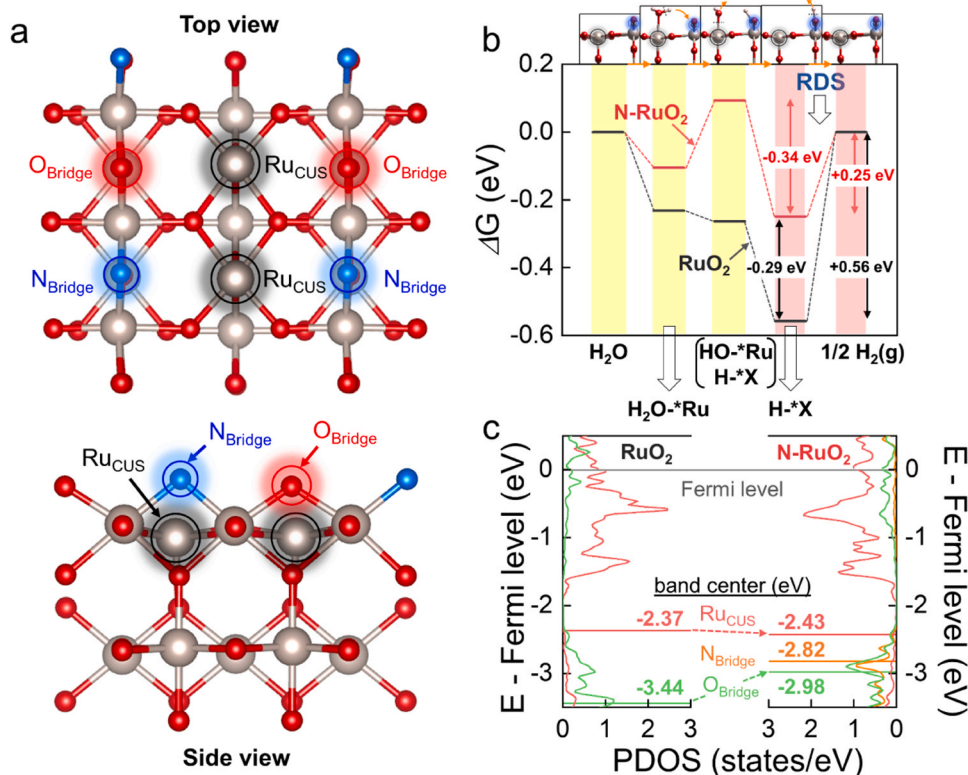
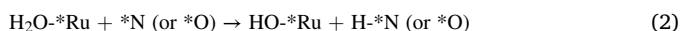


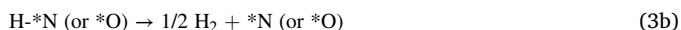
Fig. 4. DFT calculation. (a) The model structure of the nitrogen-doped ruthenium oxide (N<sub>Bridge</sub>-RuO<sub>2</sub>) selected as the most stable configuration among three possible structures (Fig. S14): Gray = Ru; Red = O; Blue = N; CUS = coordinatively unsaturated sites. Nitrogen atoms replaced the bridge oxygen sites between Ru atoms on the surface. (b) Free energy ( $\Delta G$ ) diagram. \*X = \*N or \*O. (c) Projected density of states (PDOS) of N<sub>Bridge</sub>-RuO<sub>2</sub> and undoped RuO<sub>2</sub>. The d-band centers of Ru<sub>CUS</sub> and the p-band centers of O<sub>Bridge</sub> and N<sub>Bridge</sub> were indicated.



### Splitting.



### Desorption.



It should be notified that two different active sites were involved in the HER mechanism: the coordinatively unsaturated surface ruthenium atom site ( $* \text{Ru}_{\text{CUS}}$  or  $* \text{Ru}$  in the above equation) and the surface oxygen or nitrogen atom site bridging two ruthenium ( $* \text{O}_{\text{Bridge}}$  and  $* \text{N}_{\text{Bridge}}$  or  $* \text{O}$  and  $* \text{N}$  in the above equation). The oxygen atom of a water molecule was adsorbed on  $* \text{Ru}_{\text{CUS}}$ , which was confirmed by electron energy loss spectroscopy (EELS) [50]. One of the hydrogen atom of the adsorbed species ( $\text{H}_2\text{O}^* \text{Ru}_{\text{CUS}}$ ) was co-adsorbed on the neighboring  $* \text{O}_{\text{Bridge}}$  or  $* \text{N}_{\text{Bridge}}$  and then the adsorbed water was dissociated to two intermediates ( $\text{HO}^* \text{Ru}_{\text{CUS}}$  and  $\text{H}^* \text{N}_{\text{Bridge}}$  or  $\text{H}^* \text{O}_{\text{Bridge}}$ ). The surface intermediates were desorbed from their corresponding active sites for HER. The same active sites including  $* \text{Ru}_{\text{CUS}}$  and  $* \text{O}_{\text{Bridge}}$  were mentioned in hydrogen oxidation reaction (HOR) on  $\text{RuO}_2$  (110) [51]. A similar HER mechanism including two different *metal* active sites was proposed [14,52,53] while the role of an anion as an active site was reported (sulfur in  $\text{MoS}_2$ ) [54–56].

Hydrogen desorption from  $* \text{O}$  or  $* \text{N}$  was considered as the rate-determining step for all catalysts because the highest  $\Delta G_{\text{H}}$  uphill was involved in the step (Fig. 4b). The free energy of the hydrogen surface intermediate sitting on the  $\text{O}_{\text{Bridge}}$  of  $\text{RuO}_2$  ( $\Delta G_{\text{H}}^* \text{O}$ ) decreased from +0.56 eV to +0.25 eV when the oxygen was replaced by nitrogen in  $\text{N}_{\text{Bridge}}\text{-RuO}_2$  ( $\Delta G_{\text{H}}^* \text{N}$ ). The projected densities of states (PDOS) of Ru binding with N and O were compared (Fig. 4c). The  $\text{N}_{\text{Bridge}}$  doping increased the p-band center of  $\text{O}_{\text{Bridge}}$  from −3.44 eV to −2.98 eV.

Moreover, the p-band center of  $\text{N}_{\text{Bridge}}$  was more positive than those of  $\text{O}_{\text{Bridge}}$  (−2.82 eV). The nitrogen of  $\text{N}_{\text{Bridge}}\text{-RuO}_2$ , electron-poorer than the oxygen of  $\text{RuO}_2$ , bound proton weaker so that the hydrogen binding energy went to a more positive value closer to the energy of the desorbed state for hydrogen evolution. Resultantly, hydrogen desorption from the nitrogen site was more favored.

On the other hand, the  $* \text{Ru}$  site was modified to facilitate hydroxyl desorption from  $\text{HO}^* \text{Ru}$  by nitrogen doping. The nitrogen doping shifted the d-band center of  $\text{RuO}_2$  toward the negative direction from −2.37 eV to −2.43 eV, indicating that Ru in  $\text{N-RuO}_2$  had more electrons than Ru in undoped  $\text{RuO}_2$  (Fig. 4c) [57]. The less electronegative N (electronegativity = 3.04) withdrew less electrons from Ru (2.2) than the more electronegative O (3.44) did. Therefore, the nitrogen doping increased the electron density of the Ru of  $\text{RuO}_2$  as discussed above in XANES data (Fig. 2d and e). The excess electrons of electron-rich Ru in  $\text{N-RuO}_2$  facilitated hydroxyl desorption from  $\text{HO}^* \text{Ru}$  by filling the anti-bonding between the intermediate species and the ruthenium active site [57]. The hydroxyl intermediate on  $\text{HO}^* \text{Ru}$  were more easily desorbed from  $* \text{Ru}$  in the presence of nitrogen dopant. The thermodynamic driving force for hydroxyl desorption for  $\text{N-RuO}_2$  was greater than that of its undoped counterpart: the free energy change of the step 3 (Eq. 3a) =  $\Delta G_{\text{H}}^* \text{X} - \Delta G_{\text{HO}}^* \text{Ru}$  with  $\text{H}^* \text{X} = -0.34$  eV for  $\text{N-RuO}_2$  versus −0.29 eV for  $\text{RuO}_2$  (Fig. 4b).

### 3.5. Water splitting

Water was split in a H-type electrolysis cell for demonstrating the superior HER activities of the nitrogen-doped ruthenium oxide shown by the rotating disk electrode in the three-electrode cell configuration (Fig. 5a). The nitrogen-doped ruthenium oxide catalysts embedded in nitrogen-doped carbon matrix ( $\text{N}_{0.9}\text{-RuO}_2@ \text{NC}$  and  $\text{N}_{0.5}\text{-RuO}_2@ \text{NC}$ ) were compared with their undoped counterpart ( $\text{RuO}_2/\text{C}$ ) and the reference HER catalyst (Pt/C). The HER catalysts loaded on carbon

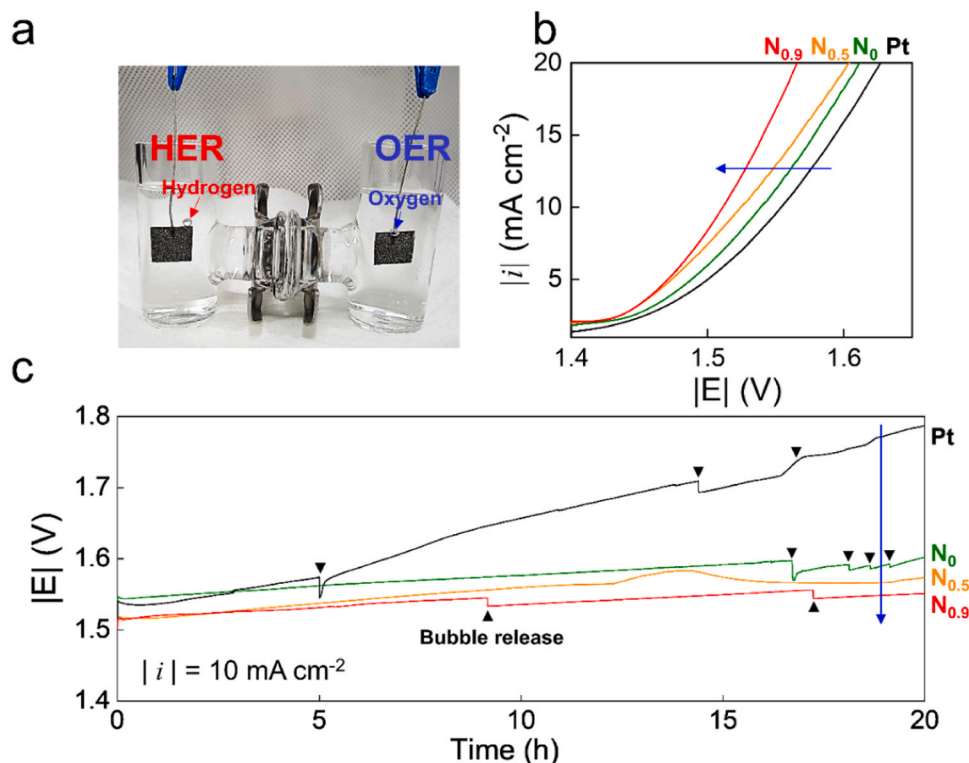


**Fig. 5.** Water electrolysis.  $\text{N}_{0.9} = \text{N}_{0.9}\text{-RuO}_2@ \text{NC}$ ;  $\text{N}_{0.5} = \text{N}_{0.5}\text{-RuO}_2@ \text{NC}$ ;  $\text{N}_0 = \text{RuO}_2/\text{C}$ ; Pt = Pt/C. (a) A H-type cell with two electrodes in 1 M KOH for water splitting at 1.5 V: HER electrode = catalysts-loading carbon paper (Toray,  $1 \times 1 \text{ cm}^2$ ); OER electrode =  $\text{RuO}_2$  on carbon paper (Toray,  $1 \times 1 \text{ cm}^2$ ). (b) HER polarization curves. Cell voltages were recorded between the HER and OER electrodes. (c) Galvanostatic durability. Cell voltages were measured at  $10 \text{ mA cm}^{-2}$  for 20 h.

paper were used as the HER electrode. A commercially available RuO<sub>2</sub> on carbon paper was used as the OER catalyst on the counter OER electrode. During the water splitting operation, bubbles were significantly released from both HER and OER electrodes.

As expected, the highly nitrogen-doped ruthenium oxide (N<sub>0.9</sub>-RuO<sub>2</sub>@NC) was significantly superior to the less nitrogen-doped counterpart (N<sub>0.5</sub>-RuO<sub>2</sub>@NC), the undoped counterpart (RuO<sub>2</sub>@C) and Pt/C in terms of HER kinetics for water splitting (Fig. 5b). The smallest overpotential was required for obtaining the same current when the N<sub>0.9</sub>-RuO<sub>2</sub>@NC was employed. Also, the water splitting durability was confirmed in the presence of the N<sub>0.9</sub>-RuO<sub>2</sub>@NC (Fig. 5c). Hydrogen was continuously produced by applying 10 mA cm<sup>-2</sup> to the H-type cells for 20 h for the catalyst durability test. The initial cell voltage of the N<sub>0.9</sub>-RuO<sub>2</sub>@NC was 11 mV lower than that of Pt/C. The cell voltage based on the N<sub>0.9</sub>-RuO<sub>2</sub>@NC did not change significantly along the operational time course. Other ruthenium oxide catalysts were durable while the voltage was developed in the presence of Pt/C. The voltage difference between N<sub>0.9</sub>-RuO<sub>2</sub>@NC and Pt/C was amplified to 236 mV after the 20 h water splitting operation. The relative voltage increases after 20 h operation were: 3.1% for N<sub>0.9</sub>-RuO<sub>2</sub>@NC < 3.6% for N<sub>0.5</sub>-RuO<sub>2</sub>@NC < 5.2% for RuO<sub>2</sub>@C < 17.9% for Pt/C.

#### 4. Conclusion

Ruthenium oxide was tuned to move its hydrogen binding energy ( $\Delta G_{H^*}$ ) from negative to near zero. Nitrogen-doped ruthenium oxides (N-RuO<sub>2</sub>) were prepared by pyrolyzing nitrogen-containing polymers with a ruthenium precursor. A highly nitrogen-doped RuO<sub>2</sub> (N<sub>0.9</sub>-RuO<sub>2</sub>@NC) having a high degree of the Ru-N intimacy (Ru-N CN = 0.9) was prepared from Pyrd-PVA-CN whose pyrrolidone moiety was *strongly* coordinated to ruthenium ion in the precursor solution prior to calcination. From PVA-CN without the pyrrolidone moiety as the nitrogen-containing *weak*-coordination precursor, on the other hand, a less nitrogen-doped RuO<sub>2</sub> (N<sub>0.5</sub>-RuO<sub>2</sub>@NC with Ru-N CN = 0.5) was synthesized. The nitrogen doping guaranteeing the Ru-N intimacy significantly improved the HER electroactivity of RuO<sub>2</sub> catalysts. The HER activity increased along Pt/C < RuO<sub>2</sub>@C < N<sub>0.5</sub>-RuO<sub>2</sub>@NC < N<sub>0.9</sub>-RuO<sub>2</sub>@NC. The dual active center mechanism based on the DFT calculation results supported that the HER activity was possibly improved by replacing oxygen atom in RuO<sub>2</sub> by nitrogen. The less electronegative nature of nitrogen (when compared with oxygen) decreased the free energy uphill required for the desorption of hydrogen intermediate species sitting on the nitrogen (H\*<sub>N</sub> to 1/2 H<sub>2</sub> + \*<sub>N</sub>) to make the desorption process more favored. Also, the nitrogen dopant facilitated the desorption of OH<sup>-</sup> from the ruthenium site (HO\*<sub>Ru</sub> + e<sup>-</sup> to HO<sup>-</sup> + \*<sub>Ru</sub>) since the less electronegative nitrogen withdrew less electrons from the ruthenium site.

#### CRediT authorship contribution statement

**Yeongdae Lee:** Conceptualization, Visualization, Investigation, Synthesis, Electrocatalysis, Writing – original draft. **Jang Hyuk Ahn:** DFT calculation. **Seokmin Shin:** Electrocatalysis. **Seo-Hyun Jung:** Synthesis and characterization of polymer. **Han-Saem Park:** Conceptualization. **Yoon-Gyo Cho:** Synthesis and characterization of polymer. **Dong-Gyu Lee:** Electrocatalysis. **Hoyoul Kong:** Synthesis and characterization of polymer. **Jun Hee Lee:** DFT calculation. **Hyun-Kon Song:** Conceptualization, Visualization, Leading, Project administration, Funding acquisition, Writing – review & editing, Finalization.

#### Declaration of Competing Interest

The authors declare that they have no known competing financial interests or personal relationships that could have appeared to influence the work reported in this paper.

#### Acknowledgments

This work was supported by MOTIE (Open Lab (KIAT): P0002068; Package: 20010282), Korea; NRF (Nano/Material: 2021M3D1A2A047042; Climate: 2019M1A2A2065614; Material Innovation: 2020M3H4A3081874), Korea; UNIST (1.200092.01), Korea. J. H.L. acknowledges the support of Basic Research Laboratory (NRF2017R1A4A1015323), Korea. Beamline 6D of PAL was used for the XAS experiments.

#### Appendix A. Supplementary data

Morphology characterization (HRTEM, XRD, XPS, XANES, and EXAFS fitting of N-doped RuO<sub>2</sub>@NC and RuO<sub>2</sub>@C), theoretical calculation (DFT) and electrochemical analysis (cyclic voltammograms, Tafel plots).

#### Appendix B. Supporting information

Supplementary data associated with this article can be found in the online version at doi:10.1016/j.apcatb.2021.120873.

#### References

- [1] X. Zou, Y. Zhang, Noble metal-free hydrogen evolution catalysts for water splitting, *Chem. Soc. Rev.* 44 (2015) 5148–5180, <https://doi.org/10.1039/c4cs00448e>.
- [2] H. Jin, C. Guo, X. Liu, J. Liu, A. Vasileff, Y. Jiao, Y. Zheng, S.Z. Qiao, Emerging two-dimensional nanomaterials for electrocatalysis, *Chem. Rev.* 118 (2018) 6337–6408, <https://doi.org/10.1021/acs.chemrev.7b00689>.
- [3] J. Hou, Y. Wu, B. Zhang, S. Cao, Z. Li, L. Sun, Rational design of nanoscale architectures for electrocatalytic water splitting, *Adv. Funct. Mater.* 29 (2019) 1–39, <https://doi.org/10.1002/adfm.201808367>.
- [4] Q. Gao, W. Zhang, Z. Shi, L. Yang, Y. Tang, Structural design and electronic modulation of transition-metal-carbide electrocatalysts toward efficient hydrogen evolution, *Adv. Mater.* 31 (2019) 1–35, <https://doi.org/10.1002/adma.201802880>.
- [5] J. Zhu, L. Hu, P. Zhao, L.Y.S. Lee, K.-Y. Wong, Recent advances in electrocatalytic hydrogen evolution using nanoparticles, *Chem. Rev.* 120 (2020) 851–918, <https://doi.org/10.1021/acs.chemrev.9b00248>.
- [6] H.B. Gray, Powering the planet with solar fuel, *Nat. Chem.* 1 (2009) 7, <https://doi.org/10.1038/nchem.141>.
- [7] C.G. Morales-Guio, L.-A. Stern, X. Hu, Nanostructured hydrotreating catalysts for electrochemical hydrogen evolution, *Chem. Soc. Rev.* 43 (2014) 6555–6569, <https://doi.org/10.1039/C3CS60468C>.
- [8] Y. Jiao, Y. Zheng, M. Jaroniec, S.Z. Qiao, Design of electrocatalysts for oxygen- and hydrogen-involving energy conversion reactions, *Chem. Soc. Rev.* 44 (2015) 2060–2086, <https://doi.org/10.1039/C4CS00470A>.
- [9] J. Greeley, T.F. Jaramillo, J. Bonde, I. Chorkendorff, J.K. Nørskov, Computational high-throughput screening of electrocatalytic materials for hydrogen evolution, *Nat. Mater.* 5 (2006) 909–913, <https://doi.org/10.1038/nmat1752>.
- [10] Y. Abghoui, E. Skúlason, Hydrogen evolution reaction catalyzed by transition-metal nitrides, *J. Phys. Chem. C* 121 (2017) 24036–24045, <https://doi.org/10.1021/acs.jpcc.7b06811>.
- [11] A. Eftekhari, Electrocatalysts for hydrogen evolution reaction, *Int. J. Hydrog. Energy* 42 (2017) 11053–11077, <https://doi.org/10.1016/j.ijhydene.2017.02.125>.
- [12] M. Zeng, Y. Li, Recent advances in heterogeneous electrocatalysts for the hydrogen evolution reaction, *J. Mater. Chem. A* 3 (2015) 14942–14962, <https://doi.org/10.1039/C5TA02974K>.
- [13] Y. Zheng, Y. Jiao, Y. Zhu, L.H. Li, Y. Han, Y. Chen, A. Du, M. Jaroniec, S.Z. Qiao, Hydrogen evolution by a metal-free electrocatalyst, *Nat. Commun.* 5 (2014) 1–8, <https://doi.org/10.1038/ncomms4783>.
- [14] I.T. McCrum, M.T.M. Koper, The role of adsorbed hydroxide in hydrogen evolution reaction kinetics on modified platinum, *Nat. Energy* 5 (2020) 891–899, <https://doi.org/10.1038/s41560-020-00710-8>.
- [15] R. Ye, Y. Liu, Z. Peng, T. Wang, A.S. Jalilov, B.I. Yakobson, S.H. Wei, J.M. Tour, High performance electrocatalytic reaction of hydrogen and oxygen on ruthenium nanoclusters, *ACS Appl. Mater. Interfaces* 9 (2017) 3785–3791, <https://doi.org/10.1021/acsami.6b15725>.
- [16] D.H. Kwon, M.S. Okyay, S.J. Kim, J.P. Jeon, H.J. Noh, N. Park, J. Mahmood, J. B. Baek, Ruthenium anchored on carbon nanotube electrocatalyst for hydrogen production with enhanced Faradaic efficiency, *Nat. Commun.* 11 (2020) 1–10, <https://doi.org/10.1038/s41467-020-15069-3>.
- [17] H.-S. Park, J. Yang, M.K. Cho, Y. Lee, S. Cho, S.-D. Yim, B.-S. Kim, J.H. Jang, H.-K. Song, RuO<sub>2</sub> nanocluster as a 4-in-1 electrocatalyst for hydrogen and oxygen electrochemistry, *Nano Energy* 55 (2019) 49–58, <https://doi.org/10.1016/j.nanoen.2018.10.017>.
- [18] H. Sun, J.-M. Yang, J.-G. Li, Z. Li, X. Ao, Y.-Z. Liu, Y. Zhang, Y. Li, C. Wang, J. Tang, Synergistic coupling of NiTe nanorods with RuO<sub>2</sub> and NiFe-LDH layers for high-efficiency electrochemical-/photovoltage-driven overall water splitting, *Appl.*

- Catal. B Environ. 272 (2020), 118988, <https://doi.org/10.1016/j.apcatb.2020.118988>.
- [19] R. JASINSKI, A new fuel cell cathode catalyst, *Nature* 201 (1964) 1212–1213, <https://doi.org/10.1038/2011212a0>.
- [20] M. Lefèvre, E. Proietti, F. Jaouen, J.-P. Dodelet, Iron-based catalysts with improved oxygen reduction activity in polymer electrolyte fuel cells, *Science* 324 (2009) 71–74, <https://doi.org/10.1126/science.1170051>.
- [21] K. Gong, F. Du, Z. Xia, M. Durstock, L. Dai, Nitrogen-doped carbon nanotube arrays with high electrocatalytic activity for oxygen reduction, *Science* 323 (2009) 760–764, <https://doi.org/10.1126/science.1168049>.
- [22] L. Qu, Y. Liu, J.-B. Baek, L. Dai, Nitrogen-doped graphene as efficient metal-free electrocatalyst for oxygen reduction in fuel cells, *ACS Nano* 4 (2010) 1321–1326, <https://doi.org/10.1021/nn901850u>.
- [23] Y.J. Sa, S.O. Park, G.Y. Jung, T.J. Shin, H.Y. Jeong, S.K. Kwak, S.H. Joo, Heterogeneous Co–N/C electrocatalysts with controlled cobalt site densities for the hydrogen evolution reaction: structure–activity correlations and kinetic insights, *ACS Catal.* 9 (2019) 83–97, <https://doi.org/10.1021/acscatal.8b03446>.
- [24] S. Fang, X. Zhu, X. Liu, J. Gu, W. Liu, D. Wang, W. Zhang, Y. Lin, J. Lu, S. Wei, Y. Li, T. Yao, Uncovering near-free platinum single-atom dynamics during electrochemical hydrogen evolution reaction, *Nat. Commun.* 11 (2020) 1029, <https://doi.org/10.1038/s41467-020-14848-2>.
- [25] P. Sabhapathy, I. Shown, A. Sabbah, P. Raghunath, J.-L. Chen, W.-F. Chen, M.-C. Lin, K.-H. Chen, L.-C. Chen, Electronic structure modulation of isolated Co-N4 electrocatalyst by sulfur for improved pH-universal hydrogen evolution reaction, *Nano Energy* 80 (2021), 105544, <https://doi.org/10.1016/j.nanoen.2020.105544>.
- [26] K. Qu, Y. Zheng, X. Zhang, K. Davey, S. Dai, S.Z. Qiao, Promotion of electrocatalytic hydrogen evolution reaction on nitrogen-doped carbon nanosheets with secondary heteroatoms, *ACS Nano* 11 (2017) 7293–7300, <https://doi.org/10.1021/acsnano.7b03290>.
- [27] Y.G. Cho, S.H. Jung, S.H. Joo, Y. Jeon, M. Kim, K.M. Lee, S. Kim, J.M. Park, H. K. Noh, Y.S. Kim, J.E. Hong, S.I. Jeon, T. Kim, S.K. Kwak, H. Kong, H.K. Song, A metal-ion-chelating organogel electrolyte for le Chatelier depression of Mn 3+ disproportionation of lithium manganese oxide spinel, *J. Mater. Chem. A* 6 (2018) 22483–22488, <https://doi.org/10.1039/c8ta08560a>.
- [28] J.H. Zagal, F. Bedioui, J.-P. Dodelet, N4-Macrocyclic Metal Complexes, Springer, New York, New York, NY, 2006, <https://doi.org/10.1007/978-0-387-28430-9>.
- [29] J.H. Zagal, F. Bedioui, Electrochemistry of N4 Macrocyclic Metal Complexes, Springer International Publishing, Cham, 2016, <https://doi.org/10.1007/978-3-319-31172-2>.
- [30] T. Marshall-Roth, N.J. Libretto, A.T. Wrobel, K.J. Anderton, M.L. Pegis, N.D. Ricke, T. Van Voorhis, J.T. Miller, Y. Surendranath, A pyridinic Fe-N4 macrocycle models the active sites in Fe/N-doped carbon electrocatalysts, *Nat. Commun.* 11 (2020) 5283, <https://doi.org/10.1038/s41467-020-18969-6>.
- [31] H. Liang, S. Brüller, R. Dong, J. Zhang, X. Feng, K. Müllen, Molecular metal–Nx centres in porous carbon for electrocatalytic hydrogen evolution, *Nat. Commun.* 6 (2015) 7992, <https://doi.org/10.1038/ncomms8992>.
- [32] X. Qiu, C. Burda, Chemically synthesized nitrogen-doped metal oxide nanoparticles, *Chem. Phys.* 339 (2007) 1–10, <https://doi.org/10.1016/j.chemphys.2007.06.039>.
- [33] M.D. Calisir, M. Gungor, A. Demir, A. Kilic, M.M. Khan, Nitrogen-doped TiO2 fibers for visible-light-induced photocatalytic activities, *Ceram. Int.* 46 (2020) 16743–16753, <https://doi.org/10.1016/j.ceramint.2020.03.250>.
- [34] Y.-S. Kim, Y.-G. Cho, D. Odkhuu, N. Park, H.-K. Song, A physical organogel electrolyte: characterized by in situ thermo-irreversible gelation and single-ion-predominant conduction, *Sci. Rep.* 3 (2013) 1917, <https://doi.org/10.1038/srep01917>.
- [35] Y.G. Cho, C. Hwang, D.S. Cheong, Y.S. Kim, H.K. Song, Gel/Solid polymer electrolytes characterized by in situ gelation or polymerization for electrochemical energy systems, *Adv. Mater.* 31 (2019) 1–12, <https://doi.org/10.1002/adma.201804909>.
- [36] F.M. Albertí, J.J. Fiol, A. García-Raso, M. Torres, A. Terrón, M. Barceló-Oliver, M. J. Prieto, V. Moreno, E. Molins, Ruthenium(III) and iridium(III) complexes with nicotine, *Polyhedron* 29 (2010) 34–41, <https://doi.org/10.1016/j.poly.2009.05.082>.
- [37] X.Y. Yi, Y. Liang, C. Li, Recent developments in ruthenium nitrido complexes, *RSC Adv.* 3 (2013) 3477–3486, <https://doi.org/10.1039/c2ra21949b>.
- [38] X. Yang, J. Zheng, M. Zhen, X. Meng, F. Jiang, T. Wang, C. Shu, L. Jiang, C. Wang, A linear molecule functionalized multi-walled carbon nanotubes with well dispersed PtRu nanoparticles for ethanol electro-oxidation, *Appl. Catal. B Environ.* 121–122 (2012) 57–64, <https://doi.org/10.1016/j.apcatb.2012.03.027>.
- [39] J.V. Rojas, M. Toro-Gonzalez, M.C. Molina-Higgins, C.E. Castano, Facile radiolytic synthesis of ruthenium nanoparticles on graphene oxide and carbon nanotubes, *Mater. Sci. Eng. B Solid-State Mater. Adv. Technol.* 205 (2016) 28–35, <https://doi.org/10.1016/j.mseb.2015.12.005>.
- [40] L.X. Chen, T. Rajh, Z. Wang, M.C. Thurnauer, XAFS studies of surface structures of TiO2 nanoparticles and photocatalytic reduction of metal ions, *J. Phys. Chem. B* 101 (1997) 10688–10697, <https://doi.org/10.1021/jp971930g>.
- [41] C.I. Hiley, M.R. Lees, J.M. Fisher, D. Thompson, S. Agrestini, R.I. Smith, R. I. Walton, Ruthenium(V) oxides from low-temperature hydrothermal synthesis, *Angew. Chem. Int. Ed.* 53 (2014) 4423–4427, <https://doi.org/10.1002/anie.201310110>.
- [42] S. Riegg, A. Reller, A. Loidl, S.G. Ebbinghaus, Valence properties of Cu and Ru in titanium-substituted LnCu3Ru4O12+δ (Ln = La, Pr, Nd) investigated by XANES and TGA, *Dalton Trans.* 44 (2015) 10852–10859, <https://doi.org/10.1039/c4dt03876b>.
- [43] Y. Liu, W.E. Mustain, Evaluation of tungsten carbide as the electrocatalyst support for platinum hydrogen evolution/oxidation catalysts, *Int. J. Hydrog. Energy* 37 (2012) 8929–8938, <https://doi.org/10.1016/j.ijhydene.2012.03.044>.
- [44] Z. Pu, I.S. Amiin, Z. Kou, W. Li, S. Mu, RuP2-based catalysts with platinum-like activity and higher durability for the hydrogen evolution reaction at all pH values, *Angew. Chem. – Int. Ed.* 56 (2017) 11559–11564, <https://doi.org/10.1002/anie.201704911>.
- [45] T.G. Kelly, S.T. Hunt, D.V. Esposito, J.G. Chen, Monolayer palladium supported on molybdenum and tungsten carbide substrates as low-cost hydrogen evolution reaction (HER) electrocatalysts, *Int. J. Hydrog. Energy* 38 (2013) 5638–5644, <https://doi.org/10.1016/j.ijhydene.2013.02.116>.
- [46] Y. Lee, J.H. Ahn, H.Y. Park, J. Jung, Y. Jeon, D.G. Lee, M.H. Kim, E. Lee, C. Kim, Y. Kwon, H.W. Lee, J.H. Jang, J.H. Lee, H.K. Song, Support structure-catalyst electroactivity relation for oxygen reduction reaction on platinum supported by two-dimensional titanium carbide, *Nano Energy* 79 (2021), 105363, <https://doi.org/10.1016/j.nanoen.2020.105363>.
- [47] J. Yang, D. Kang, Y. Jeon, J.H. Lee, H.Y. Jeong, H.S. Shin, H.-K. Song, Sphere-to-multipod transmorphing change of nanoconfined Pt electrocatalyst during oxygen reduction reaction, *Small* 15 (2019), 1802228, <https://doi.org/10.1002/sml.201802228>.
- [48] J. Yang, S.H. Kim, S.K. Kwak, H.K. Song, Curvature-induced metal-support interaction of an islands-by-islands composite of platinum catalyst and carbon nano-onion for durable oxygen reduction, *ACS Appl. Mater. Interfaces* 9 (2017) 23302–23308, <https://doi.org/10.1021/acsmi.7b04410>.
- [49] A.A. Adeniyi, P.A. Ajibade, Exploring the ruthenium-ligands bond and their relative properties at different computational methods, *J. Chem.* 2016 (2016) 1–15, <https://doi.org/10.1155/2016/3672062>.
- [50] A. Lobo, H. Conrad, Interaction of H2O with the RuO2(110) surface studied by HREELS and TDS, *Surf. Sci.* 523 (2003) 279–286, [https://doi.org/10.1016/S0039-6028\(02\)02459-7](https://doi.org/10.1016/S0039-6028(02)02459-7).
- [51] M. Knapp, D. Crihan, A.P. Seitsonen, H. Over, Hydrogen transfer reaction on the surface of an oxide catalyst, *J. Am. Chem. Soc.* 127 (2005) 3236–3237, <https://doi.org/10.1021/ja043355h>.
- [52] Z. Zeng, K.C. Chang, J. Kubal, N.M. Markovic, J. Greeley, Stabilization of ultrathin (hydroxy)oxide films on transition metal substrates for electrochemical energy conversion, *Nat. Energy* 2 (2017) 1–9, <https://doi.org/10.1038/nenergy.2017.70>.
- [53] R. Subbaraman, D. Tripkovic, K.C. Chang, D. Strmcnik, A.P. Paulikas, P. Hirunsit, M. Chan, J. Greeley, V. Stamenkovic, N.M. Markovic, Trends in activity for the water electrolyser reactions on 3d M(Ni,Co,Fe,Mn) hydr(oxy)oxide catalysts, *Nat. Mater.* 11 (2012) 550–557, <https://doi.org/10.1038/nmat3313>.
- [54] Y. Sun, Z. Wang, Density functional theory study on the hydrogen evolution reaction in the S-rich SnS2 nanosheets, *Electrocatalysis* 11 (2020) 604–611, <https://doi.org/10.1007/s12678-020-00618-7>.
- [55] T. Zhang, H. Zhu, C. Guo, S. Cao, C.-M.L. Wu, Z. Wang, X. Lu, Theoretical investigation on the hydrogen evolution reaction mechanism at MoS2 heterostructures: the essential role of the 1T/2H phase interface, *Catal. Sci. Technol.* 10 (2020) 458–465, <https://doi.org/10.1039/C9CY01901D>.
- [56] W. Li, G. Liu, J. Li, Y. Wang, L. Ricardez-Sandoval, Y. Zhang, Z. Zhang, Hydrogen evolution reaction mechanism on 2H-MoS2 electrocatalyst, *Appl. Surf. Sci.* 498 (2019), 143869, <https://doi.org/10.1016/j.apsusc.2019.143869>.
- [57] J.K. Nørskov, F. Abild-Pedersen, F. Studt, T. Bligaard, Density functional theory in surface chemistry and catalysis, *Proc. Natl. Acad. Sci. USA* 108 (2011) 937–943, <https://doi.org/10.1073/pnas.1006652108>.